Opto-Electronic Science

ISSN 2097-0382 CN 51-1800/O4

High-intensity spatial-mode steerable frequency up-converter toward on-chip integration

Haizhou Huang, Huaixi Chen, Huagang Liu, Zhi Zhang, Xinkai Feng, Jiaying Chen, Hongchun Wu, Jing Deng, Wanguo Liang and Wenxiong Lin

Citation: Huang HZ, Chen HX, Liu HG, et al. High-intensity spatial-mode steerable frequency up-converter toward on-chip integration. *Opto-Electron Sci* **3**, 230036 (2024).

https://doi.org/10.29026/oes.2024.230036

Received: 7 October 2023; Accepted: 12 January 2024; Published online: 24 April 2024

Opto-Electronic Science

Article
April 2024, Vol. 3, No. 4

DOI: 10.29026/oes.2024.230036

High-intensity spatial-mode steerable frequency up-converter toward on-chip integration

Haizhou Huang[2], Huaixi Chen[2]*, Huagang Liu[1,3], Zhi Zhang[1], Xinkai Feng[4], Jiaying Chen[1,5], Hongchun Wu[1,5], Jing Deng[1,5], Wanguo Liang[1]* and Wenxiong Lin[1,3]*

Integrated photonic devices are essential for on-chip optical communication, optical-electronic systems, and quantum information sciences. To develop a high-fidelity interface between photonics in various frequency domains without disturbing their quantum properties, nonlinear frequency conversion, typically steered with the quadratic (χ2) process, should be considered. Furthermore, another degree of freedom in steering the spatial modes during the χ2 process, with unprecedent mode intensity is proposed here by modulating the lithium niobate (LN) waveguide-based inter-mode quasi-phase-matching conditions with both temperature and wavelength parameters. Under high incident light intensities (25 and 27.8 dBm for the pump and the signal lights, respectively), mode conversion at the sum-frequency wavelength with sufficient high output power (−7 – 8 dBm) among the TM_{01}, TM_{10}, and TM_{00} modes is realized automatically with characterized broad temperature ($\Delta T \geq 8$ °C) and wavelength windows ($\Delta\lambda \geq 1$ nm), avoiding the previous efforts in carefully preparing the signal or pump modes. The results prove that high-intensity spatial modes can be prepared at arbitrary transparent wavelength of the χ2 media toward on-chip integration, which facilitates the development of chip-based communication and quantum information systems because spatial correlations can be applied to generate hyperentangled states and provide additional robustness in quantum error correction with the extended Hilbert space.

Keywords: integrated photonics; LN waveguide; sum-frequency generation; spatial-mode steering; on-chip integration

Huang HZ, Chen HX, Liu HG et al. High-intensity spatial-mode steerable frequency up-converter toward on-chip integration. *Opto-Electron Sci* **3**, 230036 (2024).

Introduction

Integrated photonic devices, consisting of diverse waveguides (optical circuits)[1−2], microcavities[3,4], modulators[5−7], and laser sources[8−10], are essential for next-generation optical communication[11,12], optical-electronic systems[13,14], and quantum information sciences including quantum computation[15,16], quantum signal processing[17,18], and quantum sensing[19,20]. Photonics features, such as frequency, polarization, path, pulse shape, and orbital angular momentum (OAM), have been used for the functionality in space-division multiplexing[21], polarization encoding[22,23], spatial-temporal entanglement[24],

[1]Key Laboratory of Optoelectronic Materials Chemistry and Physics, Fujian Institute of Research on the Structure of Matter, Chinese Academy of Science, Fuzhou 350002, China; [2]Key Laboratory of Opto-Electronic Science and Technology for Medicine of Ministry of Education, Fujian Provincial Key Laboratory of Photonics Technology, College of Photonic and Electronic Engineering, Fujian Normal University, Fuzhou 350117, China; [3]Fujian Science & Technology Innovation Laboratory for Optoelectronic Information of China, Fuzhou 350108, China; [4]College of Digital Economy, Fujian Agriculture and Forestry University, Fuzhou 350002, China; [5]University of Chinese Academy of Sciences, Beijing 100049, China.

*Correspondence: HX Chen, E-mail: chenhx@fjnu.edu.cn; WG Liang, E-mail: wgl@fjirsm.ac.cn; WX Lin, E-mail: wxlin@fjirsm.ac.cn

Received: 7 October 2023; Accepted: 12 January 2024; Published online: 24 April 2024

OAM multiplexing and de-multiplexing[12,25,26], beam shifting and steering[27,28], among others. Gathering these features matches the current trends in maximizing the link capacity for classical long-distance communications[29] and extending the Hilbert space of quantum systems[30,31].

To develop a high-fidelity interface between photonics in various frequency domains without disturbing their quantum properties[24,32], nonlinear frequency conversion, steered with quadratic ($\chi2$) processes, should be considered. These methods could be the classical second-harmonic generation (SHG)[33,34], phase-matching-free SHG[35], difference-frequency generation[36], optical parametric oscillation[37], and nonclassical spontaneous parametric down-conversion[38,39]. Meanwhile, accompanying spatial mode conversion was observed in the ferroelectric domain engineerable potassium titanyl phosphate (KTP) and lithium niobate (LN) crystals for quasi-phase matching (QPM) because of the inter-mode dispersion of the waveguide geometric[40−43]. This nontrivial process is promising in processing both the classical and quantum signals, such as selectively de-multiplexing the invisible multi-spatial mode signals toward the visible region[44] or preparing the high-dimension quantum states[32]. For inter-mode conversion, broadband lasers, or light sources with similar wavelengths[42,45] were applied, which rendered the prepared up-converted or down-converted spatial mode difficult to be discriminated because of their contiguous wavelengths[41,45]. This problem was determined using a tunable source as the fundamental wave (FW) in addition to the adjustment of the working temperature for phase matching[41]. However, the second harmonic (SH) wavelength of the spatial mode was uncontrollable with obvious shifting. By adjusting position of the FW inside a periodically poled LN (PPLN) waveguide to excite suitable FW modes[40,47], evolution in the spatial mode of the SH wave was observed, which changed from TM_{01}, TM_{10}, to TM_{00} within a short temperature range from 23 °C to 26 °C[48]. However, because the intensity of the generated space-mode was extremely weak under poor incident fundamental wave intensity (-13.5 dBm at 800 nm in ref.[40] and 7 dBm at 1066 nm in ref.[46]), detail adjustment to the incident light for rigorous mode-matching was required to selectively inspire the specific spatial mode for detection. Although spatial mode of the fundamental light can be easily prepared with a bulky spatial mode modulator[44], these measures inevitably prohibit development of the spatial mode steering device for on-chip integration with other fundamental elements, such as the mircolasers[49] and fail to meet the rapid development in chip-based integrated optics.

In addition to commonly up/down converting the spatial mode between the FW and SH[41,47], the parametric process, dominated by three-wave mixing, is appealing, which provides an additional degree of freedom in selecting the mixing wavelength to satisfy the inter-mode QPM condition and making the target wavelength controllable without spectral drifting or broadening[43−45]. Furthermore, during a sum–frequency generation (SFG) process, the incident infrared signals could be selectively mode converted at the visible region, which can be easily detected and has ultra-low signal noise[50].

In this paper, we demonstrate a high-intensity spatial-mode steering scheme during the SFG processes with a PPLN waveguide by separately manipulating the waveguide temperature and the wavelength of the mixing wave, which takes place under sufficient high incident light intensities (2~4 order of magnitudes higher than that in the previous reports[40,46]) without carefully adjusting incident lights or using the spatial light modulator[40,44,48]. Mode conversions at the SFG wavelength, among TM_{01}, TM_{10}, and TM_{00} modes, are realized at each characterized broad temperature ranges ($\Delta T \geq 8$ °C) and wavelength ranges ($\Delta\lambda \geq 1$ nm). The resulting mode intensities, un-reported in relevant literatures[40−48], are within −7 – 8 dBm, which are sufficiently high for on-chip processing of both classical and quantum signals.

Results and discussion

Theoretical modeling

Among $\chi2$ optical materials, LN has received considerable attention in integrated optics because of its sufficiently high second nonlinear coefficient (d_{33} = 27 pm/V[51]), engineerable ferroelectric domain for QPM, strong Pockels effect for electro-optical modulation[5], and moderate third-order nonlinearity (1.6×10^{-21} m^2/V^2) for acousto-optical modulation[52] or Raman processes[53]. In a few-mode PPLN waveguide with a poling period of Λ, nonlinear conversion among the signal (λ_S), pump (λ_P), and up-converted (λ_F) waves is defined by the QPM condition, which is determined by the effective refractive indices n_S^{ml}, n_P^{uv}, and n_F^{jk} of the waveguide. Here, jk, nv, and ml define the numbers of the modal points of the

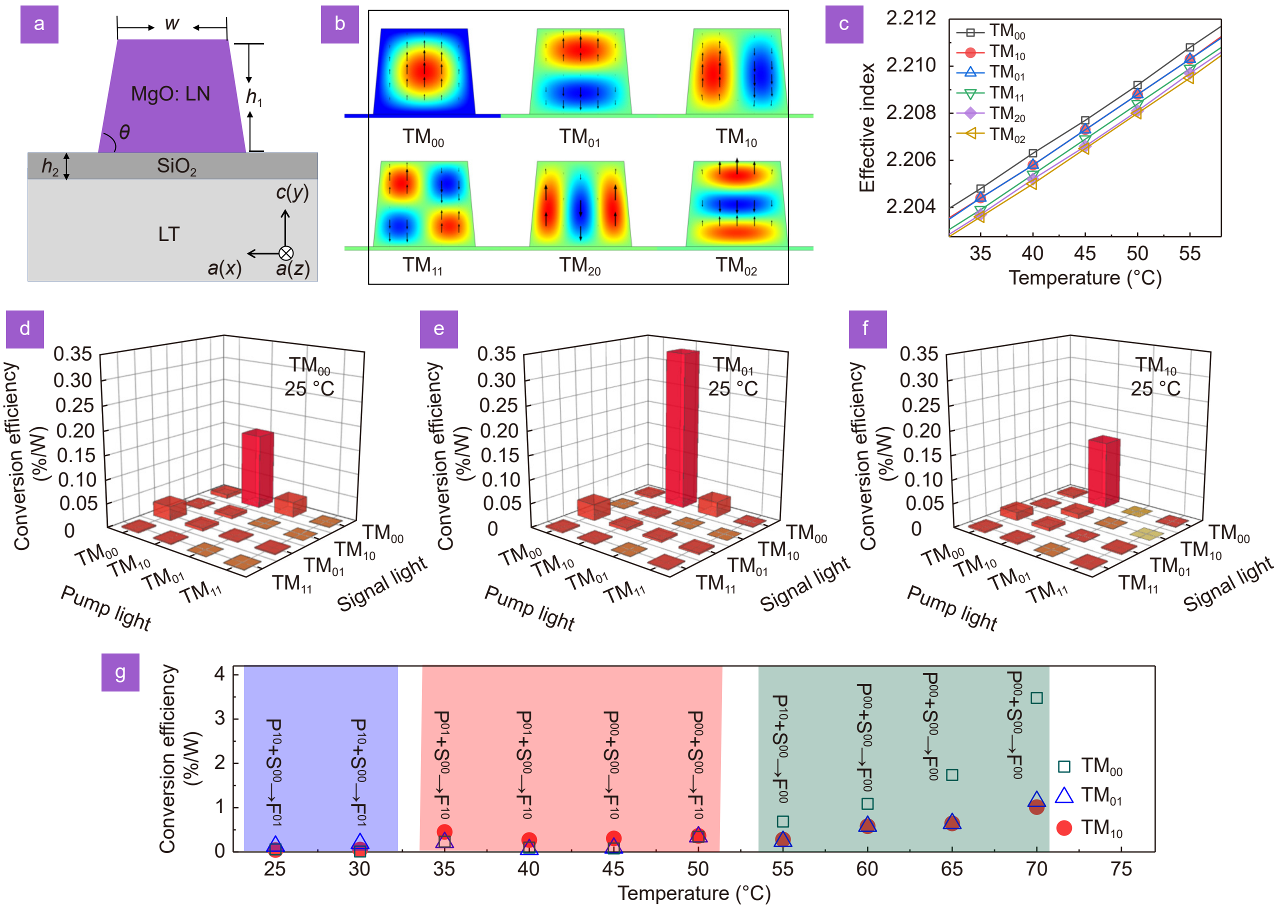

Fig. 1 | (**a**) Geometric of the prepared Z-cut PPMgLN waveguide with a poling period of 10.2 μm, where w= 11.2 μm, h_1 = 10.9 μm, h_2 = 0.5 μm, and θ = 75.1°. (**b**) Characteristic mode profiles of the SFG light at 25°C, described by the *y*-component of the electric field, where the arrows indicate directions of the electric field. (**c**) Effective indices for the TM modes of the SFG light, as the functions of the waveguide temperature. (**d–f**) Theoretical conversion efficiencies (CEs) by coupling among TM_{00}, TM_{01}, TM_{10}, and TM_{11} modes of the high-intensity pump and signal lights for the SFG lights with (d) TM_{00}. (e) TM_{01}, and (f) TM_{10} modes, respectively. (**g**) Predicted temperature conditions for producing the TM_{00} (F^{00}, cyan area), TM_{10} (F^{10}, red area), and TM_{01}(F^{01}, blue area) modes of the SFG light by comparing the maximum CE.

signal (S), pump (P), and SFG (F) lights along the horizontal and vertical directions. The effective index of the spatial modes can be linearly changed by the outer temperature (~2.989×10^{-4}/°C) because of the thermo-optical coefficient of the LN wafer (Fig. 1(c)) and enhanced by the waveguide geometric (Fig. 1(a)). Figure 1(b) lists the first six spatial modes of λ_F = 598.47 nm at 25 °C (see the enumerated mode profiles for λ_S = 1552.6 nm and λ_P = 973.85 nm in Tables S2–S4 in the Supplementary information). We consider Type-0 QPM to use the maximum nonlinear coefficient d_{33} of the PPLN waveguide, in which the dominant TM mode with the electric field parallel to the waveguide height can be excited. With the calculated effective indices, the temperature-dependent inter-mode QPM equation can be described as follows:

$$\Delta(T) = \frac{n_F^{jk}(T)}{\lambda_F} - \frac{n_P^{uv}(T)}{\lambda_P} - \frac{n_S^{ml}(T)}{\lambda_S} - \frac{1}{\Lambda} \,. \tag{1}$$

Since the signal and pump lights are with high-intensity and approximately undepleted inside the waveguide, the conversion efficiency (CE) for spatial mode $\lambda_F{}^{jk}$ at a given temperature is (see detailed derivation in the Supplementary information) as follows:

$$\eta_{\mathrm{theo}}^{jk}(T) = \frac{8\pi^2 L^2 d_{\mathrm{eff}}^2}{n_S^{ml} n_P^{uv} n_F^{jk} \varepsilon_0 c \lambda_F^2} \Phi(x,y,T) \mathrm{sinc}^2\left(\frac{\Delta k L}{2}\right), \tag{2}$$

where d_{eff} is the effective nonlinear coefficient of the LN crystal, ε_0 is the permittivity, c the speed of light, and Δk = $2\pi\Delta(T)$, and $\Phi(x, y, T)$ indicates the overlap integral among modes $\lambda_S{}^{ml}$, $\lambda_P{}^{uv}$, and $\lambda_F{}^{jk}$ at temperature T (see Supplementary information Eq. S6).

According to theoretical results (Fig. 1(d–f)), coupling among modes TM_{01}, TM_{10}, and TM_{00} of the pump and signal and SFG lights dominates the spatial mode conversion process during frequency up-conversion. That is, at 25 °C, dominant processes $\lambda_S{}^{00} + \lambda_P{}^{00} \to \lambda_F{}^{00}$, $\lambda_S{}^{00} + \lambda_P{}^{01}$

→ λ_F^{01} and λ_S^{00} + λ_P^{10} → λ_F^{10} contribute for the potential TM_{00}, TM_{01}, and TM_{10} modes with conversion efficiencies of 0.158%/W, 0.333%/W, and 0.143%/W, respectively. Thus, the resulting SFG mode under 25 °C is at TM_{01}, which automatically takes place under high incident pump and signal light intensities without specifically modulating spatial modes of the incident lights as the conventional manners. With the theoretical process, we could detail the spatial mode to be produced at a given temperature, and characteristic broad steerable temperature ranges for modes TM_{01}, TM_{10}, and TM_{00} are predicted (Fig. 1(g)).

Experimental characterization

To verify theoretical prediction, we prepared a few-mode PPLN waveguide array consisting of seven waveguides with a length of 30 mm (Fig. 2(d)), which was diffusion-boned on a lithium tantalate (LT) wafer with the assistance of a SiO_2 layer (see Fig. S1 for the fabrication flowchart). The third waveguide, with well-protected cutting edge and lowest loss (0.29 dB/cm), was used throughout the experiment process (Fig. 2(e)). The ridge waveguide is characterized with a width of 11.2 μm and height of 10.9 μm to support at least 47, 11, and 50 eigenmodes at the pump, signal, and SFG wavelengths, respectively, at which three typical SFG modes (TM_{00}, TM_{01}, and TM_{10}), meeting the temperature controlled inter-mode QPM conditions are distinguished on a white broad (Fig. 2(b)). As with the designed poling period, Λ was measured to be 10.2 μm using the microscopy image (Fig. 2(f)). We coupled signal light at the c-band from a tunable Erbium fiber-based master oscillator power-amplifier and pump light at 973.85 nm from a single-mode fiber-coupled diode laser into the ridge waveguide (Fig. S3), which was mounted inside a thermoelectric cooler (Fig. 2(a)). The pump and signal lights have maximum output powers of 25 dBm and 27.8 dBm respectively to implement an automatic spatial mode steering process, without specially

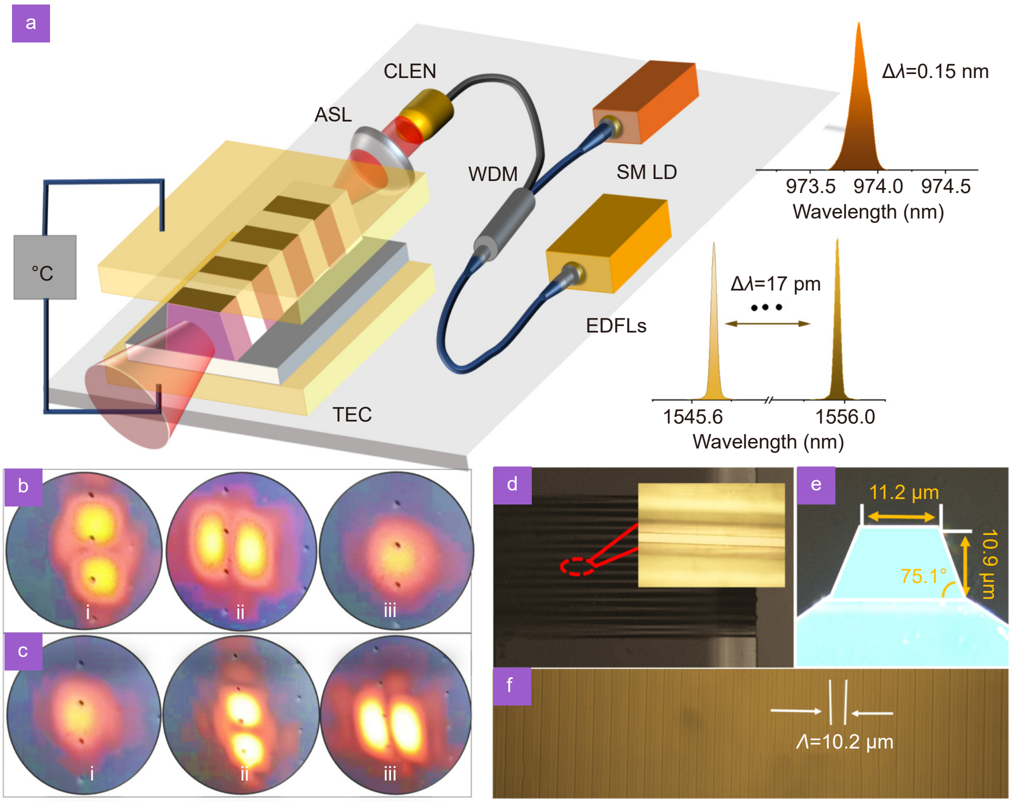

Fig. 2 | (**a**) Schematic of the temperature/wavelength-dependent spatial mode steerable SFG device. (**b**) In the temperature steering scheme, the detected up-conversion lights with (i) TM_{01}, (ii) TM_{10}, and (iii) TM_{00} modes at 30°C, 40°C, and 60°C, respectively, on a white broad. (**c**) In the wavelength steering scheme, the detected SFG lights with (i) TM_{00}, (ii) TM_{01}, and (iii) TM_{10} modes at 597.46, 597.99, and 598.41 nm, respectively, on a white broad. (**d**) Microscope image of the fabricated PPMgLN waveguide array on an LT wafer (Inset: detail profile of the third waveguide). (**e**) Cross-section view of the fifth waveguide selected in the experiments. (**f**) The fabricated polling structure with a period of 10.2 μm. EDFLs, Erbium-ion doped fiber laser system; SM LD, single-mode fiber-coupled diode laser; WDM, wavelength division multiplexer; CLEN, collimating lens; ASL, aspherical lens; TEC, thermoelectric cooler.

preparing the signal or pump modes in advance. Moreover, to avoid other potential spatial modes at the SFG wavelength caused by the broad bandwidth of the pump and signal waves[45,47], their bandwidths are narrow and with values of 0.15 and 0.017 nm, respectively. Therefore, pure TM_{01}, TM_{10}, and TM_{00} modes are prepared stably at temperature ranges from 25 °C to 32 °C, 35 °C to 43 °C, and 54 °C to 70 °C, respectively (Fig. 2(b)). By tuning the signal wavelength from 1546 to 1556 nm, evolution in the spatial mode recurs and changes from TM_{00}, TM_{01}, to TM_{10} (Fig. 2(c)). Both temperature- and wavelength-dependent steering methods are appealing in integrated optics through preparing target spatial modes with accessible wavelengths in the quantum or classical optical networks and overcoming the growing complexity of quantum information protocols.

On fixing the incident power of the pump light at 25 dBm, we measured the power curves of the SFG process at various temperatures from 25 °C to 70 °C (Fig. 3(a)) at which the signal wavelength was 1552.6 nm. The spatial mode did not change during each power scaling process at a given TEC temperature. Under an incident signal power of 27.8 dBm, Fig. 3(b) depicts the maximum SFG power versus the working temperature. The regions for pure spatial mode are denoted with colors. Figure 3(c) displays the evolution of SFG efficiency (denoting by $\eta_{exp}= 100{\cdot}P_{SFG}/P_P/P_S$), which is consistent with the calculation result by denoting the maximum CE among F_{01}, F_{10}, and F_{00} (Fig. 1(g)) as the theoretical efficiency $\eta_{cal} = \max(\eta_{F10}, \eta_{F01}, \eta_{F10})$. Controlling the waveguide temperature from 25 °C to 70 °C, the spatial mode begins with TM_{01} and subsequently changes from TM_{01} to TM_{10}, and TM_{10} to TM_{00} (Fig. 3(e)). Figure 3(d) depicts the width of temperature windows for TM_{01}, TM_{10}, and TM_{00} modes, with values of 8 °C, 9 °C, and 17 °C, respectively, which are sufficiently broad for a stable pure spatial mode generation. At each temperature window, the maximum SFG intensities are −3.82, −2.08, and 7.82 dBm, with corresponding conversion efficiencies of 0.21%/W, 0.29%/W, and 3.16%/W. The SFG spectrum is verified to be stabilizing at 598.47 ± 0.1 nm when changing the waveguide temperature (Fig. 3(f)).

Between adjacent spatial modes, an obvious temperature window, covering a few Celsius degrees as the transition state, exists. This window can be attributed to the

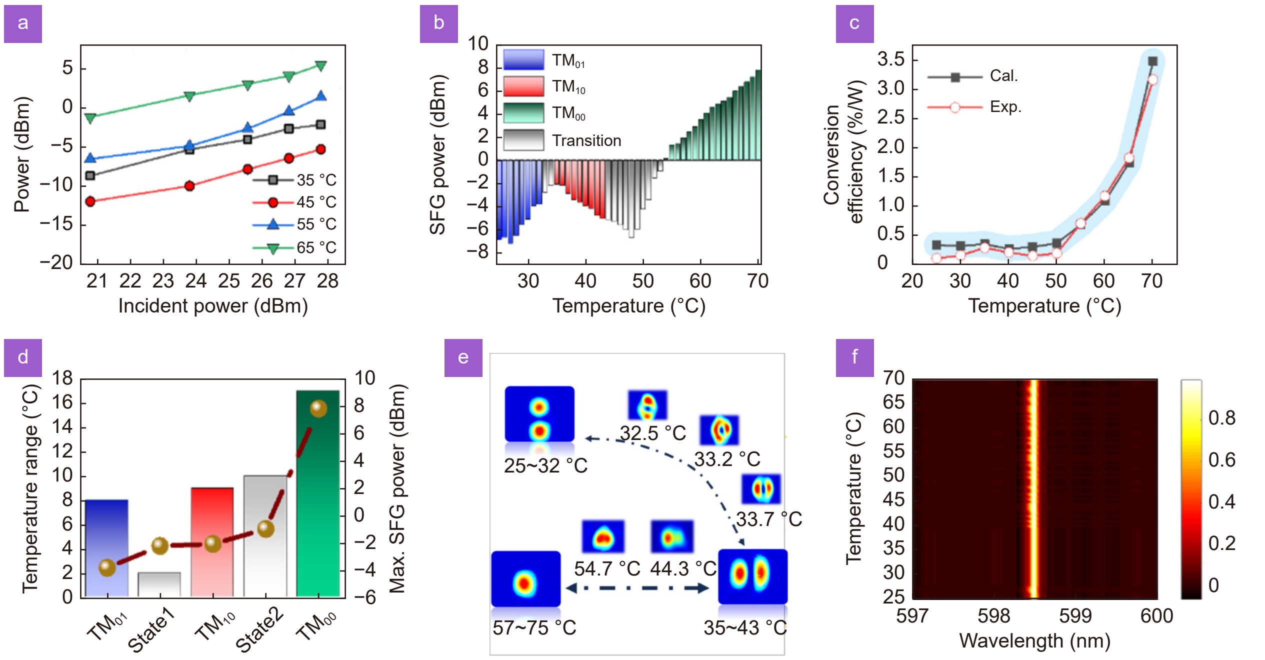

Fig. 3 | Characterizing the temperature-dependent spatial mode steering scheme in the SFG waveguide. (**a**) Power curves of the waveguide at typical temperatures of 35 °C, 45 °C, 55 °C, and 65 °C. (**b**) Evolution in SFG power under the maximum incident pump power of 27.8 dBm, in which the gray color denotes the regions without clear TM_{01}, TM_{10}, or TM_{00} modes. (**c**) Experimental efficiency ($\eta_{exp} = 100{\cdot}P_F/P_P/P_S$) and theoretical efficiency ($\eta_{cal} = \max(\eta_F^{jk}, \eta_F^{jk}, \eta_F^{jk})$) of the inter-mode up-conversion process. (**d**) Temperature windows for preparing mode TM_{01}, TM_{10}, and TM_{00}, where state1 and state2 denote the transition process from TM_{10} to TM_{01} and TM_{01} to TM_{00}, respectively. (**e**) Mode profiles captured by the CCD camera to tell the exact modes during rising the waveguide temperature. (**f**) Evolutions in the SFG wavelength during the spatial mode steerable SFG process.

competition among the spatial modes with comparable conversion efficiencies. In the first transition state, mode rotation from TM_{01} to TM_{10} occurs (Fig. 4(d)), which was first observed in an SHG PPLN waveguide (within a small temperature range of ~2 °C) and explained as the coupling between TM_{10} and TM_{01}[48]. However, in the second transition state, the rotated mode profile is distorted (Fig. 4(e)). According to the theoretical CE for modes TM_{00}, TM_{01}, and TM_{10}, we could see CE for TM_{00} gradually increases and participates in the coupling between TM_{10} and TM_{01} with the increased waveguide temperature (Fig. 4(c)). Since the mode overlap integral $\Phi(x, y, T)$ for TM_{00}, TM_{01}, and TM_{10} is relatively stable (Fig. 4(b)), the resulting mixing mode patterns in transition states are originated by the temperature-dependent QPM efficiencies (denoted by sinc($\Delta kL/2$)) (Fig. 4(a)). We derive the mixing mode amplitude $E_F(T)$ as follows:

$$E_F^i(T) = \sum_{jk} A_F^{jk} E_F^{jk}(T) \ , \tag{3}$$

where i denotes the i^{th} transition state, and jk the fundamental TM modes for the SFG light. Here jk = 00, 01, and 10 is selected and $A_F{}^{jk}$ denotes the complex amplitudes for mode jk. Denoting $A_F{}^{01} = 1$, we obtain $A_F{}^{10} = r_1 e^{i\theta_1}$ and $A_F{}^{00} = r_2 e^{i\theta_2}$, where ($r_1 = \eta_{10}/\eta_{01}$, θ_1) and ($r_2 = \eta_{00}/\eta_{01}$, θ_2) are the relative amplitudes and phase angles of $A_F{}^{01}$ and $A_F{}^{00}$ to $A_F{}^{10}$, respectively. In the first state, as the CE of TM_{00} is sufficiently small to be ignored, mixing mode patterns between TM_{10} and TM_{01} are computed and classified as the quasi-TM01, quasi-TM10, and highly coupling modes, in Fig. S4(a). The coupling modes occur at $0.7 \le r_1 \le 3$ with 0.8 rad $\le \theta_1 \le$ 2.2 rad or −2.2 rad $\le \theta_1 \le$ −0.8 rad. Therefore, the coupling mode patterns at 32.5 °C and 33.7 °C can be reproduced by setting (r_1, θ_1) as (0.77, π/3) and (1, −π) (Fig. 4(d)). In the second transition state, the mixing mode pattern is blurred because of the growing CE of TM_{00}. We address this three-mode coupling state by initializing the mode pattern under the two-mode coupling condition before sweeping parameters between r_2 and θ_2 (Table S5). In addition to setting (r_1, θ_1) as (1.14, π/2), (r_2, θ_2) = (1.2, −π/2) is selected (Fig. 4(e)). In the third transition state, TM_{00} dominates the mixing mode, where the mode profile becomes convergent into a quasi TM_{00} mode with the increased waveguide temperature (Fig. 4(f)) and is insensitive to r_1, θ_1, and θ_2 (Fig. S5).

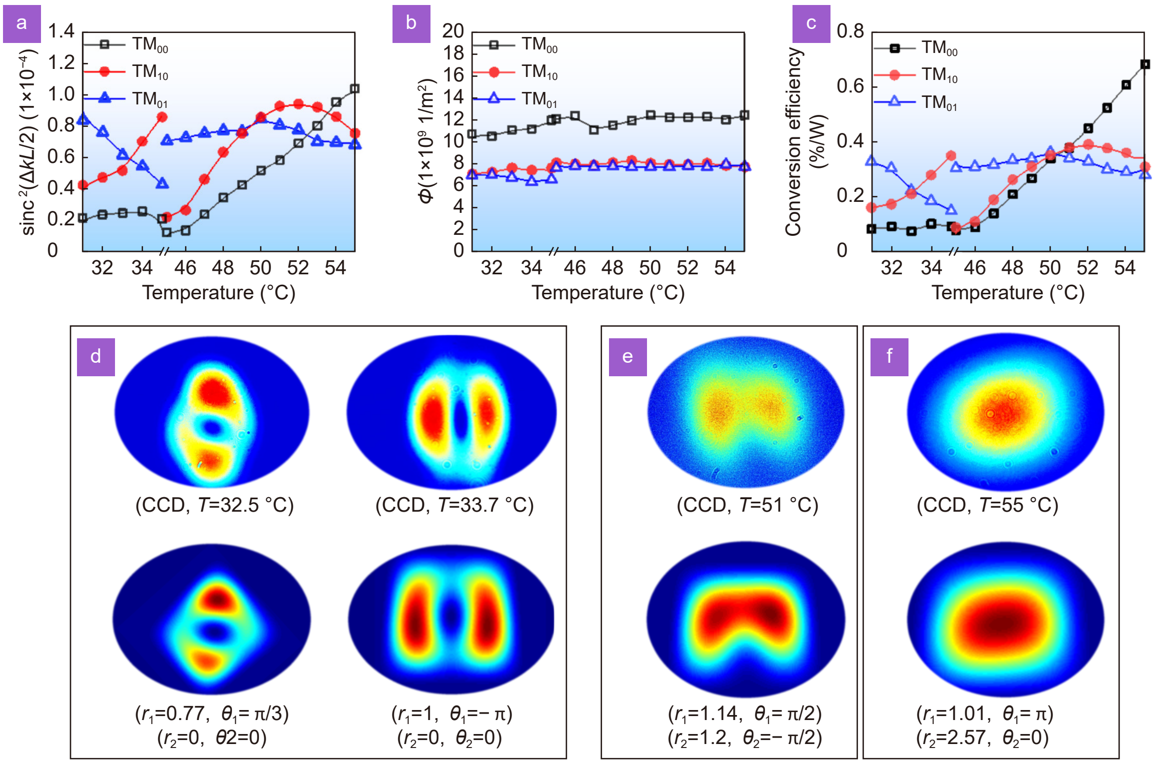

Fig. 4 | Transition states from two-mode coupling (first state), three-mode coupling (second state), to quasi TM_{00} mode (third state). (**a–c**) Evolutions of the (a) inter-mode QPM efficiency (sinc($\Delta KL/2$)), (b) integral, and (c) conversion efficiency for TM_{00}, TM_{10}, and TM_{01}, respectively. (**d–f**) Typical mixing mode pattern in the (d) first state, (e) second state, and (f) third state, respectively, where the upper picture is experimentally captured by a CCD camera, and the bottom picture is reproduced based on Eq. (3) with $I = |E_F|^2$.

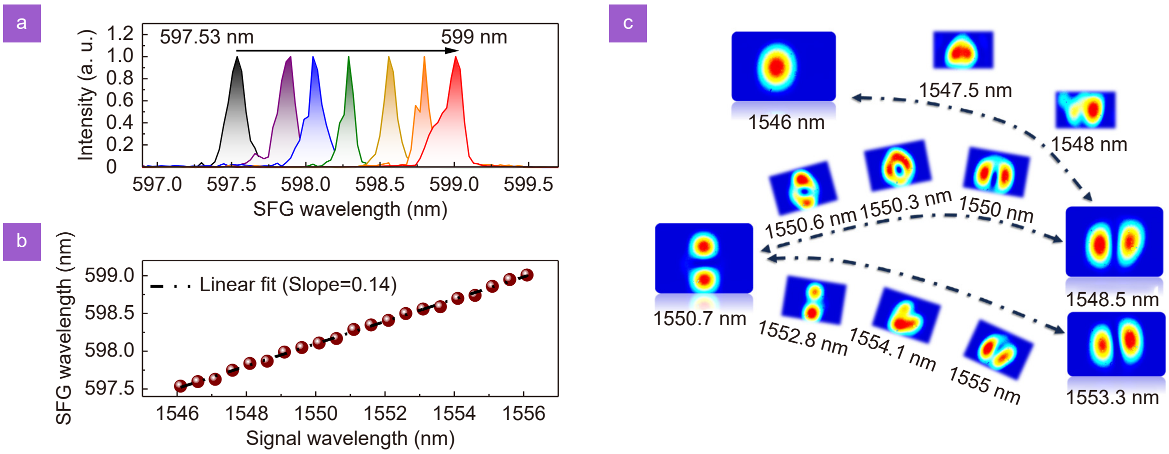

Fig. 5 | Characterizing the wavelength-dependent spatial mode steering scheme in the SFG waveguide. (**a**, **b**) The changed SFG wavelength by increasing the signal wavelength from 1546 to 1556 nm: (a) spectral profiles, (b) fitted slop rate $\Delta\lambda_P/\Delta\lambda_S$ = 0.14; (c) at waveguide temperature of 25 °C, the evolution of the spatial mode from TM_{00} to TM_{10}, TM_{10} to TM_{01}, and TM_{01} to TM_{10}.

Changing the signal wavelength from 1546 to 1556 nm, the SFG wavelength changes from 597.54 to 599 nm (Fig. 5(a)), where the slop rate is fit to be $\Delta\lambda_P/\Delta\lambda_S$ = 0.14. Mode conversion occurs during red shifting the SFG wavelength (Fig. 5(c)). Theoretically, this method can be described by the inter-mode QPM condition (Eq. (1)), where the changed signal and pump wavelengths and the resulting effective indexes are considered:

$$\Delta(T,\lambda_P,\lambda_S)=\frac{n_F^{jk}(T,\lambda_F)}{\lambda_F}-\frac{n_P^{uv}(T,\lambda_P)}{\lambda_P}-\frac{n_S^{ml}(T,\lambda_S)}{\lambda_S}-\frac{1}{\Lambda}\,, \tag{4}$$

here, $\lambda_F = 1/(1/\lambda_P+1/\lambda_S)$. Experimentally, Fig. 6(a) illustrates the measured SFG power during turning the signal wavelength at various waveguide temperatures (see Tables S6–S9 for the evolution processes of the spatial mode at 35 °C, 45 °C, 55 °C, and 65 °C, respectively), where the wavelength range for pure TM_{01}, TM_{10}, and TM_{00} modes is denoted. As with the temperature-dependent steering scheme, characterized broad wavelength windows to prepare the pure spatial modes by changing the signal wavelength are displayed (Fig. 6(b)). With the working temperature and incident mixing wavelengths, a 2D route map for preparing demanded spatial mode with up/down-conversion wavelength within the transparent window of the QPM $\chi 2$ media can be determined.

Conclusions

We have comprehensively demonstrated a high-intensity spatial-mode steerable frequency up-converter in both temperature and wavelength manipulating methods. Stable TM_{01}, TM_{10}, and TM_{00} modes at the SFG wavelength could be prepared automatically within a few-mode PPLN waveguide without prefabricating the spatial modes of the incident signal and pump lights by adjusting the incident combined lights or using a spatial light modulator. This result is appealing for on-chip integration with the microlasers such as distributed feedback laser (DFB)[49] or semiconductor optical amplifier[54]. The conversion processes can be theoretically explained by the competition among the SFG spatial modes under a high-intensity three wave mixing process described with the inter-mode QPM model, where a considerable broad temperature range with a width of approximately 8 °C and a waveband width of approximately 1 nm is displayed for the prepared spatial modes. The maximum mode switching speed is theoretically limited by the frequency-switching speed of the tunable pump or signal sources.

Moreover, because of the sufficiently high pump and signal light intensities, output power for the prepared up-converted spatial modes is within −7 to 8 dBm (200 μW to 6.3 mW), which has not been recorded in other literatures due to the poor fundamental wave intensity. This method is sufficiently high for on-chip preparation of the high-dimensional quantum information carriers in extending the Hilbert space and can be used in long-distance quantum communication and hyperentangled photon generation for increasing information capacity, improving the noise resistance, and making the quantum cryptographic schemes difficult to hack despite errors. Furthermore, the study has the potential in other functional devices including de-multiplexing the multi-mode signal by frequency conversion or encoding the target

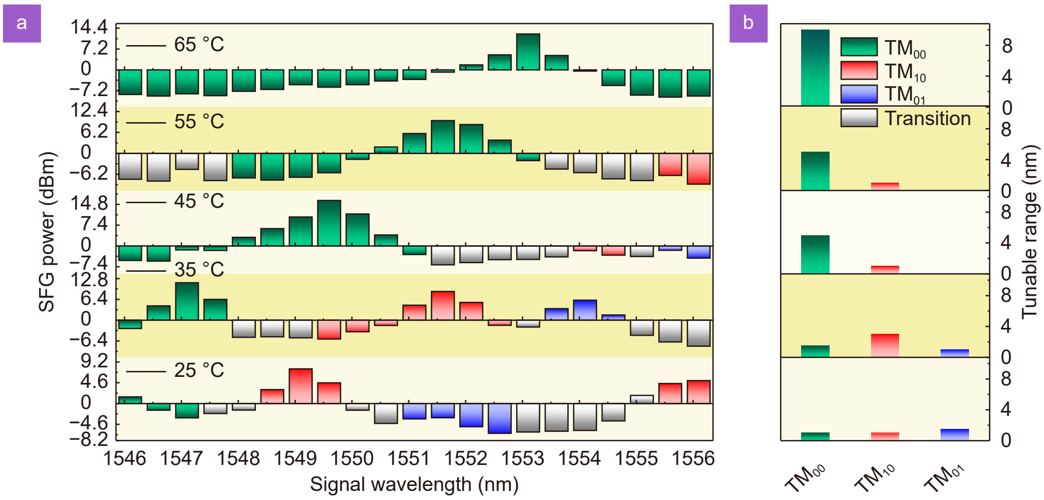

Fig. 6 | (**a**) Evolution in SFG power at varied waveguide temperature under an incident pump and signal powers of 25.1 and 27.8 dBm, respectively, where characterized regions for the TM_{00}, TM_{01}, and TM_{10} modes are denoted with cyan, red, and blue colors, respectively. (**b**) Wavelength windows for preparing the spatial mode during red shifting the SFG wavelength.

wavelength with characterized mode pattern[55]. Unlimited by the SFG scheme, the automatic spatial mode conversion process could also be implemented by differential frequency generation or optical parameter oscillation, which extends the desired wavelengths within transparent windows of the ferroelectric $\chi2$ media from ultra-violet to mid-infrared regions.

References

1. Lu XY, Li Q, Westly DA et al. Chip-integrated visible–telecom entangled photon pair source for quantum communication. *Nat Phys* **15**, 373–381 (2019).
2. Xie YW, Hong SH, Yan H et al. Low-loss chip-scale programmable silicon photonic processor. *Opto-Electron Adv* **6**, 220030 (2023).
3. Chen YP, Yin Y, Ma LB et al. Recent progress on optoplasmonic whispering-gallery-mode microcavities. *Adv Opt Mater* **9**, 2100143 (2021).
4. Liu J, Bo F, Chang L et al. Emerging material platforms for integrated microcavity photonics. *Sci China Phys Mech* **65**, 104201 (2022).
5. Li MX, Ling JW, He Y et al. Lithium niobate photonic-crystal electro-optic modulator. *Nat Commun* **11**, 4123 (2020).
6. Zhang M, Buscaino B, Wang C et al. Broadband electro-optic frequency comb generation in a lithium niobate microring resonator. *Nature* **568**, 373–377 (2019).
7. He MB, Xu MY, Ren YX et al. High-performance hybrid silicon and lithium niobate Mach-Zehnder modulators for 100 Gbit s^{-1} and beyond. *Nat Photonics* **13**, 359–364 (2019).
8. Tran MA, Zhang C, Morin TJ et al. Extending the spectrum of fully integrated photonics to submicrometre wavelengths. *Nature* **610**, 54–60 (2022).
9. Aghaeimeibodi S, Desiatov B, Kim JH et al. Integration of quantum dots with lithium niobate photonics. *Appl Phys Lett* **113**, 221102 (2018).
10. Li NX, Chen GY, Ng DKT et al. Integrated lasers on silicon at communication wavelength: a progress review. *Adv Opt Mater* **10**, 2201008 (2022).
11. Mizuno T, Miyamoto Y. High-capacity dense space division multiplexing transmission. *Opt Fiber Technol* **35**, 108–117 (2017).
12. Khonina SN, Kazanskiy NL, Butt MA et al. Optical multiplexing techniques and their marriage for on-chip and optical fiber communication: a review. *Opto-Electron Adv* **5**, 210127 (2022).
13. Dong M, Clark G, Leenheer AJ et al. High-speed programmable photonic circuits in a cryogenically compatible, visible-near-infrared 200 mm CMOS architecture. *Nat Photonics* **16**, 59–65 (2022).
14. Liao K, Chen Y, Yu ZC et al. All-optical computing based on convolutional neural networks. *Opto-Electron Adv* **4**, 200060 (2021).
15. Wang JW, Paesani S, Ding YH et al. Multidimensional quantum entanglement with large-scale integrated optics. *Science* **360**, 285–291 (2018).
16. Paesani S, Ding YH, Santagati R et al. Generation and sampling of quantum states of light in a silicon chip. *Nat Phys* **15**, 925–929 (2019).
17. Crespi A, Ramponi R, Osellame R et al. Integrated photonic quantum gates for polarization qubits. *Nat Commun* **2**, 566 (2011).
18. Qiang XG, Zhou XQ, Wang JW et al. Large-scale silicon quantum photonics implementing arbitrary two-qubit processing. *Nat Photonics* **12**, 534–539 (2018).
19. Lee SY, Ihn YS, Kim Z. Quantum illumination via quantum-enhanced sensing. *Phys Rev A* **103**, 012411 (2021).
20. Crawford SE, Shugayev RA, Paudel HP et al. Quantum sensing for energy applications: review and perspective. *Adv Quantum Technol* **4**, 2100049 (2021).
21. Yim J, Chandra N, Feng XL et al. Broadband continuous supersymmetric transformation: a new paradigm for transformation optics. *eLight* **2**, 16 (2022).
22. Carletti L, Zilli A, Moia F et al. Steering and encoding the polarization of the second harmonic in the visible with a monolithic $LiNbO_3$ metasurface. *ACS Photonics* **8**, 731–737 (2021).
23. Lin ZJ, Lin YM, Li H et al. High-performance polarization management devices based on thin-film lithium niobate. *Light Sci Appl* **11**, 93 (2022).

24. Kumar S, Zhang H, Kumar P et al. Spatiotemporal mode-selective quantum frequency converter. *Phys Rev A* **104**, 023506 (2021).
25. Guo YH, Zhang SC, Pu MB et al. Spin-decoupled metasurface for simultaneous detection of spin and orbital angular momenta via momentum transformation. *Light Sci Appl* **10**, 63 (2021).
26. Meng WJ, Hua YL, Cheng K et al. 100 Hertz frame-rate switching three-dimensional orbital angular momentum multiplexing holography via cross convolution. *Opto-Electron Sci* **1**, 220004 (2022).
27. Shang JM, Chen HJ, Sui Z et al. Electro-optic high-speed optical beam shifting based on a lithium niobate tapered waveguide. *Opt Express* **30**, 14530–14537 (2022).
28. Xu Y, Zheng KP, Shang JM et al. Wavefront shaping for reconfigurable beam steering in lithium niobate multimode waveguide. *Opt Lett* **47**, 329–332 (2022).
29. Li SJ, Li ZY, Huang GS et al. Digital coding transmissive metasurface for multi-OAM-beam. *Front Phys* **17**, 62501 (2022).
30. Biard H, Moreno-Pineda E, Ruben M et al. Increasing the Hilbert space dimension using a single coupled molecular spin. *Nat Commun* **12**, 4443 (2021).
31. Kruse R, Katzschmann F, Christ A et al. Spatio-spectral characteristics of parametric down-conversion in waveguide arrays. *New J Phys* **15**, 083046 (2013).
32. Feng LT, Zhang M, Xiong X et al. On-chip transverse-mode entangled photon pair source. *npj Quantum Inf* **5**, 2 (2019).
33. Li MX, Chang L, Wu L et al. Integrated Pockels laser. *Nat Commun* **13**, 5344 (2022).
34. Li Y, Huang ZJ, Qiu WT et al. Recent progress of second harmonic generation based on thin film lithium niobate [Invited]. *Chin Opt Lett* **19**, 060012 (2021).
35. Wang C, Li ZY, Kim MH et al. Metasurface-assisted phase-matching-free second harmonic generation in lithium niobate waveguides. *Nat Commun* **8**, 2098 (2017).
36. Mishra J, McKenna TP, Ng E et al. Mid-infrared nonlinear optics in thin-film lithium niobate on sapphire. *Optica* **8**, 921–924 (2021).
37. Lu JJ, Al Sayem A, Gong Z et al. Ultralow-threshold thin-film lithium niobate optical parametric oscillator. *Optica* **8**, 539–544 (2021).
38. Xue GT, Niu YF, Liu XY et al. Ultrabright multiplexed energy-time-entangled photon generation from lithium niobate on insulator chip. *Phys Rev Appl* **15**, 064059 (2021).
39. Zhao J, Ma CX, Rusing M et al. High quality entangled photon pair generation in periodically poled thin-film lithium niobate waveguides. *Phys Rev Lett* **124**, 163603 (2020).
40. Karpiński M, Radzewicz C, Banaszek K. Dispersion-based control of modal characteristics for parametric down-conversion in a multimode waveguide. *Opt Lett* **37**, 878–880 (2012).
41. Machulka R, Svozilík J, Soubusta J et al. Spatial and spectral properties of fields generated by pulsed second-harmonic generation in a periodically poled potassium-titanyl-phosphate waveguide. *Phys Rev A* **87**, 013836 (2013).
42. Mosley PJ, Christ A, Eckstein A et al. Direct measurement of the spatial-spectral structure of waveguided parametric down-conversion. *Phys Rev Lett* **103**, 233901 (2009).
43. Christ A, Laiho K, Eckstein A et al. Spatial modes in waveguided parametric down-conversion. *Phys Rev A* **80**, 033829 (2009).
44. Kumar S, Zhang H, Maruca S et al. Mode-selective image upconversion. *Opt Lett* **44**, 98–101 (2019).
45. Karpiński M, Radzewicz C, Banaszek K. Experimental characterization of three-wave mixing in a multimode nonlinear $KTiOPO_4$ waveguide. *Appl Phys Lett* **94**, 181105 (2009).
46. Lee YL, Shin W, Yu BA et al. Mode tailoring in a ridge-type periodically poled lithium niobate waveguide. *Opt Express* **18**, 7678–7684 (2010).
47. Eigner C, Padberg L, Santandrea M et al. Spatially single mode photon pair source at 800 nm in periodically poled Rubidium exchanged KTP waveguides. *Opt Express* **28**, 32925–32935 (2020).
48. Park JH, Kim WK, Jeong WJ et al. Continuous control of spatial mode rotation using second harmonic generation. *Appl Phys Lett* **97**, 191113 (2010).
49. Yu MJ, Barton III D, Cheng R et al. Integrated femtosecond pulse generator on thin-film lithium niobate. *Nature* **612**, 252–258 (2022).
50. Liu SL, Yang C, Xu ZH et al. High-dimensional quantum frequency converter. *Phys Rev A* **101**, 012339 (2020).
51. Vazimali MG, Fathpour S. Applications of thin-film lithium niobate in nonlinear integrated photonics. *Adv Photonics* **4**, 034001 (2022).
52. Cai LT, Mahmoud A, Khan M et al. Acousto-optical modulation of thin film lithium niobate waveguide devices. *Photonics Res* **7**, 1003–1013 (2019).
53. Yu MJ, Okawachi Y, Cheng R et al. Raman lasing and soliton mode-locking in lithium niobate microresonators. *Light Sci Appl* **9**, 9 (2020).
54. Snigirev V, Riedhauser A, Lihachev G et al. Ultrafast tunable lasers using lithium niobate integrated photonics. *Nature* **615**, 411–417 (2023).
55. Hou JF, Situ GH. Image encryption using spatial nonlinear optics. *eLight* **2**, 3 (2022).

Acknowledgements

We are grateful for financial supports from National Key Research and Development Program of China (2021YFB3602500), Self-deployment Project of Fujian Science & Technology Innovation Laboratory for Optoelectronic Information of China (2021ZZ101), and National Natural Science Foundation of China (Grant Nos. 62275247 and 61905246).

Author contributions

HZ Huang: Methodology, Investigation, Visualization, Writing–original draft; HX Chen： Device preparing, Data curation, Investigation, Writing–review & editing; HG Liu：Data curation, Writing–review & editing; Z Zhang, XK Feng, and JY Chen: Data curation, Visualization; HC Wu and J Deng: Formal analysis, Visualization; WG Liang: Supervision, Writing–review & editing; WX Lin: Conceptualization, Supervision.

Competing interests

The authors declare no competing financial interests.

Supplementary information

Supplementary information for this paper is available at https://doi.org/10.29026/oes.2024.230036